Journal of Membrane Science 661 (2022) 120957

Contents lists available at ScienceDirect

Journal of Membrane Science

journal homepage: www.elsevier.com/locate/memsci

A scalable method to fabricate high-performance biomimetic membranes for seawater desalination: Incorporating pillar[5]arene water nanochannels into the polyamide selective layer

Yu Jie Lim [a,b,c], Gwo Sung Lai [a], Yali Zhao [a], Yunqiao Ma [a,c,d], Jaume Torres [a,e], Rong Wang [a,b,*]

[a] Singapore Membrane Technology Center, Nanyang Environment and Water Research Institute, Nanyang Technological University, 637141, Singapore
[b] School of Civil and Environmental Engineering, Nanyang Technological University, 639798, Singapore
[c] Interdisciplinary Graduate Programme, Graduate College, Nanyang Technological University, 637553, Singapore
[d] School of Chemical and Biomedical Engineering, Nanyang Technological University, 637459, Singapore
[e] School of Biological Sciences, Nanyang Technological University, 637551, Singapore

ARTICLE INFO

Keywords:
Water nanochannels
Biomimetic membrane
Peptide-attached (pR)-pillar[5]arenes
Reverse osmosis
Seawater desalination

ABSTRACT

In this work, we explored the practicability of a nanochannel-based biomimetic membrane (NBM) incorporating pillar[5]arene water channels for seawater reverse osmosis (SWRO) desalination. Two classes of peptide-attached biomimetic channels, (pR)-pillar[5]arenes (pRPH) and (pS)-pillar[5]arenes (pSPH) were integrated into the selective layer of SWRO membranes *via* interfacial polymerization on the top side of a polysulfone (PSf) support membrane. Here, pSPH is a non-identical stereoisomer of pRPH and was used as a negative control to pRPH to elucidate the flux enhancement effect contributed by pRPH. The optimized NBM presented a water permeability of 2.52 L m^{-2} h^{-1} bar^{-1} and 99.5% rejection under SWRO testing conditions of 50 bar applied pressure and 32,000 mg/L NaCl as feed solution. The 62% permeability increment with reference to the control membrane is hypothesized to originate from hybrid polyamide layers that were rougher with more voids (higher effective surface area and lower hydraulic resistance for water transport) as well as the conceivable water transport pathways provided by the pRPH channels. The simulation results from module-scale modelling suggest that the optimized NBM could lead to 7.2% savings in specific energy consumption of the membrane unit stage (or reduce the required membrane area by 25%) with respect to the commercial SWC4-LD membrane. The performance of the optimized NBM was further assessed in a one-week desalination test using an actual seawater feed gathered from an SWRO plant in Singapore. The robust NBM exhibited stable performance and ~28% higher water flux (42 L m^{-2} h^{-1}) than SWC4-LD with a comparable rejection of 99.3%, suggesting the feasibility of pillar[5]arene-based biomimetic membranes for seawater desalination.

1. Introduction

Freshwater scarcity is one of the biggest threats which mankind is facing in the 21st century. Membrane-based separation technologies have a crucial role to play in addressing this challenge since it allows us to tap on unconventional water sources through water reuse and seawater desalination. The prevalent desalination technology is reverse osmosis (RO), which occupies close to 70% of the current market share [1]. The core of an RO desalination process consists of semi-permeable membranes that allow the favored transport of water molecules over solutes when seawater is pressurized across the membranes. The current state-of-the-art seawater RO (SWRO) membranes is based on the thin-film composite (TFC) design. The selective layer of the TFC-SWRO membrane is a thin polyamide layer (~200 nm) that is typically prepared *via* an interfacial polymerization (IP) reaction between a diamine and acyl chloride [2–4]. The TFC membrane has served as an industrial gold standard since its inception almost 50 years ago [1].

After decades of research and innovation, the separation performances of the TFC-SWRO membranes have gradually improved in terms of the permeability and selectivity, rendering them to be more efficient and economical in terms of energy consumption. However, empirical evidence collated from recent upper-bound models suggest that dense

* Corresponding author. Singapore Membrane Technology Center, Nanyang Environment and Water Research Institute, Nanyang Technological University, 637141, Singapore..
E-mail address: rwang@ntu.edu.sg (R. Wang).

https://doi.org/10.1016/j.memsci.2022.120957
Received 17 July 2022; Received in revised form 23 August 2022; Accepted 24 August 2022
Available online 29 August 2022

polymeric membranes (such as those for RO and gas separations) displayed a persistent permeability-selectivity tradeoff, rendering them difficult to attain better performances beyond the current achievable standard [5–7]. In the past 15 years, supramolecular chemistry has brought about the development of water nanochannels, whereas nanotechnology has opened up the possibility to develop next-generation membranes in which water nanochannels can be embedded into the membrane selective layer to confer desired properties to the latter [8–11].

One prominent example of water channels is aquaporin (AQP), a biological nanochannel that is frequently studied because of its high intrinsic water permeability while exhibiting perfect selectivity. However, there are still intrinsic challenges related to the preservation of their activity under harsh conditions, as well as the ability to translate superb ångström scale performance into benefits at the system-level (*i.e.,* from molecular transport to successful meter-scale membranes) [12,13]. Parallel to these research efforts, more straightforward approaches involving biomimetic water channels have been proposed. The notable advantages of biomimetic channels over their biological counterparts are their higher stability, tunability, processability and cost [1,13,14]. As an example, in terms of tunability, the pore size and interior chemistry of biomimetic channels can be precisely tuned at the ångström scale to achieve salt exclusion, thereby opening the possibility to use these water channels for desalination applications. Also, the cost of synthesizing biomimetic channels is relatively low owning to its facile synthesis methods, high yields and low material costs [12].

To date, one prominent type of biomimetic channels is the peptide-attached pillar[5]arene, an unimolecular channel that possess a tubular nanostructure comprising of peptide arms appended onto the cyclic macromolecule backbone (Fig. 1(A-C)) [15–17]. The pore diameter at the constriction zone of the peptide-attached pillar[5]arene is ~0.5 nm, which permits water to be funneled through in a single-file fashion [1,18]. Coupled with its interior hydrophobicity that supports slip flow conditions, the peptide-attached pillar[5]arene channel could mimic the fast water transport observed in AQPs. Pillar[5]arenes also possess the captivating trait of 2D chirality that come about due to the revolving of benzene moieties around the methylene groups. Our research group has outlined the possibility to restrict the rotation by affixing bulky and stiff substituents onto the macrocycle backbone, thereby forming two stable isomers (peptide-attached pR- and pS-pillar[5]arenes, designated as pRPH and pSPH, respectively) that possess different mass transport properties. Readers are referred to Ref. [19] for the detailed nomenclature and properties of the pR- and pS- isomers of the planar chiral pillar[5]arene. Experimental and molecular dynamics simulations have confirmed the salt exclusion capability of pRPH while supporting fast water transport [19].

In a recent work by our research group, we have shown the successful fabrication of a nanochannel-based biomimetic membrane (NBM) incorporated with pRPH channel containing-liposomes [20]. Whilst this work has outlined the feasibility of an NBM with enhanced water permeability for brackish water RO (BWRO) application, its salt rejection of <99.0% is limited with little interest for seawater desalination. In addition, liposomes preparation is a lengthy process that involves multiple steps (lipid drying, rehydration, extrusion, etc.) with the typical preparation procedures requiring more than 1 day [20]. In the current work, we attempted to resolve these two challenges by examining the possibility to fabricate NBMs in which pillar[5]arene channels are directly immobilized into the membrane selective layer as nanoparticles (Fig. 1D). Moreover, the current work involves the study of NBMs for harsher application (SWRO), in which the applied pressure and feed salinity (50 bar and 32,000 ppm NaCl, respectively) is several times higher than that of BWRO (15 bar and 2000 ppm NaCl, respectively). Here, we envision that the pRPH channels can improve the membrane permeability by furnishing possible water transport pathways, while the water-soluble nature of pillar[5]arene derivatives can enhance the compatibility with, and dispersibility in the polyamide [21,22]. The

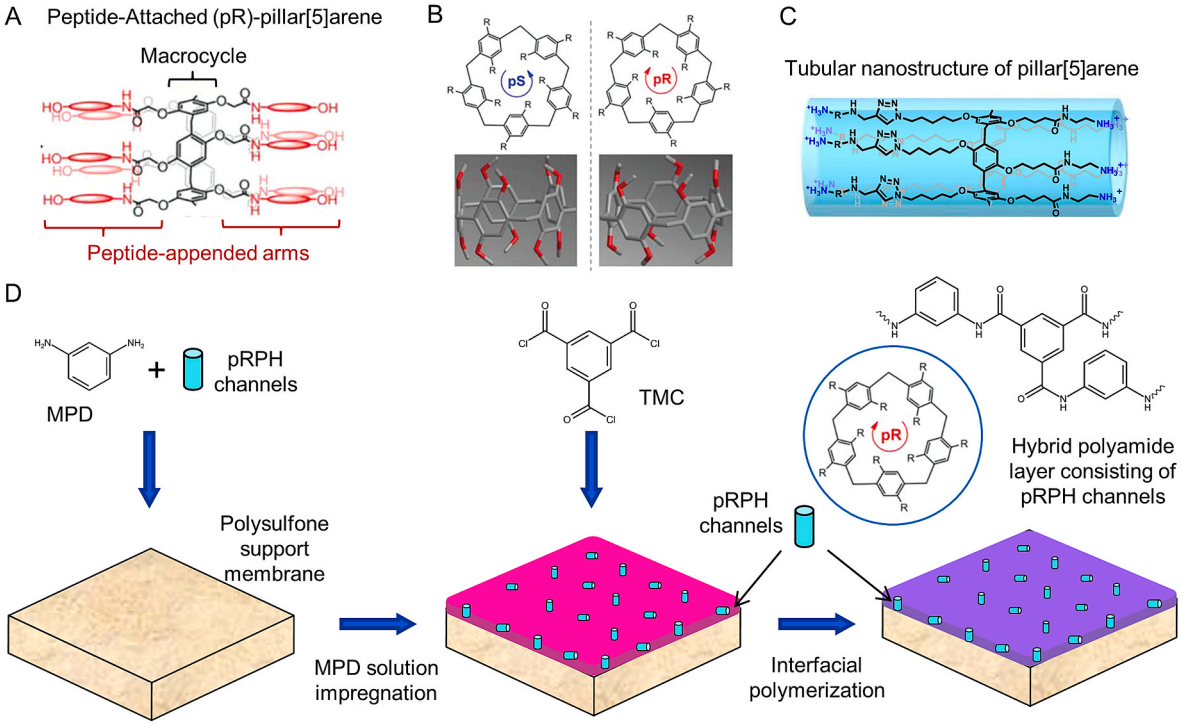

Fig. 1. (A) The structure of the pRPH channel, showing the peptide arms appended onto a macrocycle backbone. **(B)** The schematic structures of the pSPH (left) and pRPH (right) channels. (A) and (B) were modified from Ref. [19]. **(C)** An illustration of the tubular nanostructure of pillar[5]arene (modified from Ref. [18]). **(D)** Schematic illustration of the synthesis of an NBM. The support membrane is impregnated in the m-phenylenediamine (MPD) solution containing pRPH nanochannels, prior to contact with trimesoyl chloride (TMC). The pRPH channels are embedded into the hybrid polyamide layer *via* interfacial polymerization. It is surmised that the channels are randomly oriented in the polyamide layer.

latter is crucial in preventing the formation of defects in the selective layer [5]. To the best of our knowledge, this research work is the first to study the practicability of NBMs integrated with pillar[5]arene channels for SWRO application with high salt rejection of 99.5%.

2. Experimental

2.1. Materials and chemicals

In this work, all chemicals were acquired from Sigma-Aldrich unless otherwise specified. Polysulfone beads (PSf, Solvay) was dissolved in dimethylformamide (DMF) to prepare polymeric dope solutions. Phosphate buffered saline (PBS) solution and 1,2-Dioleoyl-sn-glycerol-3-phosphocholine (DOPC) lipids (Avanti Polar Lipids) were used in the preparation of liposomes. The biomimetic nanochannels, peptide-attached (pR)- and (pS)-pillar[5]arenes (pRPH and pSPH, respectively), were used to assemble channel-containing liposomes as well as in interfacial polymerization (IP). It is highlighted that the liposomes were used solely in the stopped-flow tests (*i.e.,* no liposomes were used in membrane fabrication *via* IP). The synthesis procedures of the nanochannels are detailed in our preceding research study [19]. Here, pSPH is a non-identical stereoisomer of pRPH and is used as a negative control (mutant version) to pRPH. Both biomimetic nanochannels were stored at a temperature of −18 °C prior to usage. M-Phenylenediamine (MPD), triethylamine (TEA) and camphorsulfonic acid (CSA) were used to prepare aqueous solutions in IP. Trimesoyl chloride (TMC) was dissolved in n-hexane in the preparation of the organic phase in IP. Citric acid, ethylenediamine tetraacetic acid (EDTA), sodium hydroxide (NaOH), and sodium dodecyl sulfate (SDS) were used to prepare chemical solutions. Two commercial SWRO membranes (DuPont Filmtec SW30HR and Hydranautics SWC4-LD) were assessed in this work as a point of reference.

2.2. Preparation of channel-containing liposomes for stopped-flow tests

To quantify the water permeability of the nanochannels in stopped-flow tests, both pRPH and pPSH nanochannels were used in the preparation of channel-containing liposomes using the film rehydration technique according to our previous work [20]. Firstly, nitrogen gas was used to dry 12 mL of DOPC in chloroform (concentration: 25 mg/mL) to obtain a fine lipid film on the internal surface of a round bottom flask. The flask was then put away in a vacuum desiccator (*i.e.,* a sealable enclosure) for 3 days to ensure thorough withdrawal of chloroform. Secondly, 30 mL of PBS buffer solution and a fixed quantity of nanochannels (lipid to channel ratio (LCR) of 100) were put into the flask and agitated for 50 min. The control liposome contains only DOPC without any nanochannels. Thirdly, the liposomes were subjected to three rounds of freeze-thaw and subsequently extruded three times each using Whatman microporous filters (pore sizes of 200 nm and 100 nm) in a Genizer Jacketed Liposome Extruder to obtain spherical liposomes with homogeneous size distributions [20].

2.3. Biomimetic membrane synthesis

The PSf support membranes were prepared using a pilot-scale flat-sheet membrane casting machine *via* the phase inversion method [23]. Readers are referred to our previous work for more detailed information [24]. In brief, the dope solution was prepared by dissolving 17 wt% of PSf beads in 83 wt% of DMF at 60 °C with continuous stirring. The dope solution was then degassed and cooled down to room temperature before the casting process. The dope solution was dribbled onto the polyester non-woven fabric during the casting process, in which the gate height of the casting knife and casting rate were set at 230 μm and ~6.7 cm/s, respectively. The casted films were immediately rolled into a water bath at ambient temperature to induce phase separation. The obtained support membranes were immersed in a deionized water container for 1 day to ensure complete solvent removal.

IP methodology was adopted to synthesize the membrane selective layer on the top side of the support membrane. Two solutions were utilized in the IP process: 3.5 wt/v% MPD aqueous solution and 0.16 wt/v% TMC solution dissolved in hexane. A trace amount of TEA-CSA salt (3–4 wt/v%) was included into the MPD solution as an aqueous phase additive [25,26]. In the fabrication of NBMs, nanochannels were blended into the MPD solution. A methodical optimization of the nanochannel loading was performed to pinpoint the leading performance attainable by the NBMs. Here, the baseline membrane is denoted as a TFC control membrane whereas the NBMs integrated with pRPH and pSPH nanochannels were designated as NBM-pRPH-x and NBM-pSPH-x, respectively (where x denotes the concentration (mg/L) of the nanochannels in MPD solution).

Readers are referred to a previous study by our research group for detailed information of the IP procedure [27]. Briefly, the PSf support membranes were first dipped in MPD solutions for 1 min. The surplus MPD solution was then purged off from the surface using an air-knife. Secondly, the MPD-saturated support membranes were contacted with TMC solution for 1 min to synthesize the polyamide layer. Thirdly, the membranes were placed in a 60 °C forced convection oven for 10 min to induce the curing process. Lastly, the membranes were placed in a water bath for 2 h and subsequently transferred to a 4 °C refrigerator for 12 h prior to testing.

2.4. Liposome characterization

The size distribution profiles of the liposomes were measured using a size analyzer (Zetasizer Nano ZS) *via* quasi-elastic light scattering technique. In brief, the liposomes were dispersed in PBS buffer solution (concentration: 0.2 mg/mL) and the translucent solution was transferred to a square cuvette for measurement. The water permeability of the vesicles was ascertained using a stopped-flow spectrometer (SX20, Applied Photophysics), as per reported previously [20]. The draw solution is 600 mM sucrose. The draw solution and vesicle solution were mixed in the same proportion under pressurized nitrogen gas (4 bar). To determine the shrinkage rate of the vesicles, the fitted rate constant (k) was computed using the Pro-Data SX software by fitting the data points into a single exponential function. Lastly, the water permeability of each individual vesicle is computed as follows:

$$P_f = \frac{k}{S/V_0 \times V_w \times \Delta osm} \quad (1)$$

where S/V_0 is the surface area to volume ratio of an individual vesicle, V_w is the molar volume of water (0.018 cm^3/mol), and Δosm is the osmolarity difference between the mixing solutions.

2.5. Membrane characterization

The membranes were air dried for 2 days prior to characterization experiments. An atomic force microscope (AFM), Park XE-100 (Korea) was used to analyze the surface roughness average (R_a) of the membranes. The cantilever tips used were the PPP-NCHR type (Nanosensors) with a length of 125 μm and a typical radius of curvature of less than 10 nm. The AFM images were acquired in a non-contact mode with a resolution of 256 pixels using a scan rate of 0.5–0.8 Hz for 25 μm^2 areas. The surface wettability of the membranes was evaluated using an optical contact angle measurement system (OCA 15, Dataphysics) and was presented as a contact angle averaged from six measurements. The surface structure and cross-sections of the membrane selective layers were examined using scanning electron microscopy (SEM, JEOL) at an accelerating voltage of 5 kV. Freeze cracking in liquid nitrogen was performed to inspect the cross-sections of the polyamide layer. Prior to SEM imaging, all samples were overlayed with a platinum layer at 20 mA for 100 s.

To examine the functional groups present in the membranes, the attenuated total reflection (ATR) - fourier transform infrared (FTIR) spectra was recorded on an IR Prestige-21 spectrometer [28]. The equipment contained a michelson interferometer at an incident angle of 30° and all spectra were recorded at ambient temperature in the region of 800–2000 cm^{-1}. To estimate the cross-linking degrees of the polyamide layers, XPS (X-ray photoelectron spectroscopy) characterization was used to establish the elemental compositions. Next, the C1s peak at 284.8 eV was deconvoluted in an attempt to deduce the chemical bonds in the polyamide layer, as per reported previously [20]. In brief, the C1s baseline was constrained between 280 eV and 292 eV, and subsequently the peaks were identified, and their respective atomic compositions were quantified using the CasaXPS processing software.

2.6. Performance evaluation of the SWRO membranes

The separation performances of the SWRO membranes were assessed using a crossflow filtration system equipped with permeation cells (CF042D, Sterlitech), in which the effective area of each membrane coupon is 42 cm^2. To determine the water permeability coefficient A (L m^{-2} h^{-1} bar^{-1}), the membranes were pre-compacted with deionized water at 50 bar for 2 h to attain stable permeate flux.

$$A = \frac{J_w}{(\Delta P - \Delta \pi)} \tag{2}$$

where J_w, ΔP and $\Delta \pi$ are the water flux, applied pressure and osmotic pressure difference across the SWRO membrane, respectively. Next, the feed water was replaced by synthetic seawater (32,000 ppm NaCl solution) and another 3 h of filtration was conducted to determine the salt rejection:

$$R = 1 - C_p / C_f \tag{3}$$

where C_p and C_f are the concentrations of the permeate and feed streams, respectively (units: g/L). The commercial SWRO membranes were tested under the same protocol. The feed water temperature was kept constant at 25 °C for all tests. The inverse salt permeability coefficients ($1/B$) were quantified according to the following equation:

$$\frac{1}{B} = \frac{1}{J_w} \times \left(\frac{R}{1-R}\right) \tag{4}$$

To assess the chemical stability of the optimized NBM for practical desalination application, the membranes were soaked in different solutions (for 1 h): 20 g/L citric acid (pH 2), 1 g/L NaOH (pH 12.41), 8 g/L EDTA (pH 2.77) and 0.3 g/L SDS (pH 12.42), which are common chemicals used in membrane cleaning operation [29,30]. Thereafter, they were washed thoroughly with deionized water prior to RO filtration tests. A seven-day test was conducted for the optimized NBM using actual seawater feed collected from a seawater desalination plant in Singapore (the feed was pre-treated by an ultrafiltration membrane process). The commercial SWC4-LD membrane was assessed in parallel for benchmarking purposes. Unless otherwise stated, all tests were conducted at an applied pressure of 50 bar under a crossflow velocity of 15.8 cm/s. The cation and boron concentrations of the feed and permeate streams were determined using inductively coupled plasma-optical emission spectrometry (ICP-OES, PerkinElmer Avio 550 Max), whereas the anion concentrations were acquired by ion chromatography (IC, Dionex Aquion). To ensure accurate measurements within the calibration range available in the equipment, the solutions were either diluted with water (IC) or 1% nitric acid aqueous solution (ICP-OES).

2.7. System-level modelling of an SWRO plant operating with spiral-wound elements

Assuming that the lab-scale membranes could be scaled-up to element size, we attempted to quantify the membrane performance enhancement on the energy and footprint savings achievable at a system-level by applying a module-scale model that was previously reported by our research group [31]. The salt water permeability and rejection values of the membranes obtained in the experiments were directly input into the simulation as modelling parameters. In brief, we quantified the specific energy consumption (SEC, kWh/m^3) and footprint requirement of the SWRO membrane unit (single-stage) by modelling the fluid dynamics and mass transport properties of the SWRO train, consisting of eight spiral-wound membrane elements connected in series. Each individual element is 8-inch in diameter, with a length and effective membrane area of 1.0 m and 37 m^2, respectively. The feed concentration of the SWRO stream was set at 32,000 mg/L NaCl. Both the SEC and footprint requirements were calculated under a fixed permeate recovery of 50%. Also, the SEC was computed under a fixed feed flowrate of 320 m^3/day, whereas the number of SWRO trains was calculated under a fixed inlet pressure of 70 bar and a pre-determined production capacity of 100,000 m^3/day [31].

To perform the simulation, we considered the variation in the membrane element in the axial direction and the control volume was discretized in the streamwise direction (*i.e.,* from the inlet stream to the outlet stream of an SWRO train). The pressure losses, fluid dynamics and mass balances in the streamwise direction are governed by four ordinary differential equations (ODEs), which describes the rate of change based on the mass transfer coefficient and local permeate flux. With the given boundary condition, the system of ODEs was solved iteratively using numerical integration in *MATLAB 2021a* from the inlet to the outlet stream using the trapezoidal rule and fsolve solver. The required inlet pressure, SEC, number of SWRO trains, concentration polarization factor and permeate flux were readily computed by the model and are presented as a function of recovery along the SWRO train. Readers are referred to Ref. [31] for the model validation and detailed information of the system-level modelling of an SWRO plant operating with flat-sheet spiral-wound elements.

3. Results and discussion

3.1. Characteristics of the liposomes and water permeability of pRPH channels

According to the results obtained from dynamic light scattering experiments (Fig. 2A), the channel-containing liposomes have an average size of ~116 nm with an excellent polydispersity index of 0.055. The latter is a manifestation of the uniform size distribution of the vesicles that will guarantee the accuracy of water permeability data obtained from stopped-flow experiments [20]. It is noticed that the pRPH-liposomes (LCR 100) showed a rapid increase in fluorescence at the initial stage that is accompanied by a plateau stage (k value: 236 s^{-1}, refer to Fig. 2B). The sharp increase of the signal within a minuscule duration (<0.01 s) is a manifestation of the fast conveyance of water molecules across the pRPH channels, while the following steady stage of the signal indicates that the liposomes were stable under the current solute conditions. In a striking difference, the stopped-flow curves of the DOPC liposomes and pSPH-liposomes (under a similar LCR of 100) were much more subtle (lower k values of 17–20 s^{-1}), which indicates the relatively impenetrable characteristics of the DOPC and pSPH-liposomes [20]. Based on these results, we attempted to quantify the net permeability of the liposomes under identical preparation and testing conditions.

Under a similar LCR of 100 (that is the number of channels in a liposome), the net permeability of the pRPH-incorporated vesicle is 706 μm/s, which is 13-fold higher than that of the pSPH-incorporated vesicle (56 μm/s) (Fig. 2C). Because pSPH is a non-identical stereoisomer of pRPH and is used as a negative control (mutant) to pRPH, this result demonstrates that water transport through the pRPH-liposomes is expedited by the pRPH channels [19,20]. Furthermore, the activation

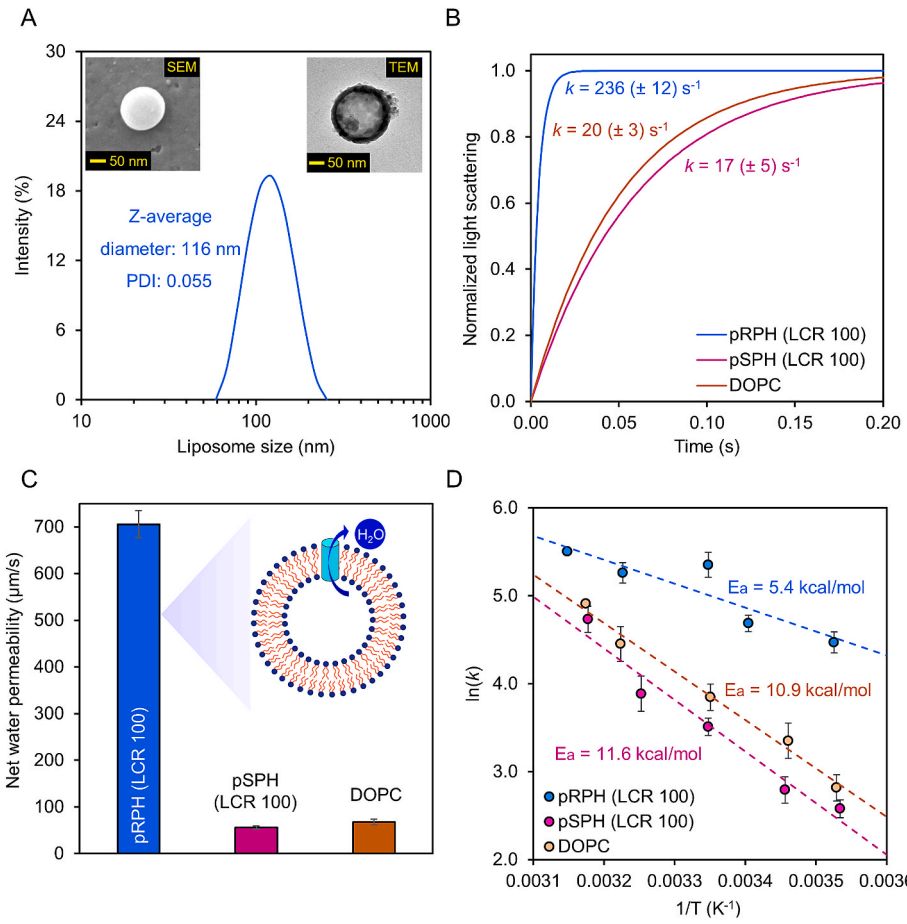

Fig. 2. (A) The size distribution of a pRPH-liposome after extrusion. The insets present the images of a pRPH-liposome observed in SEM and transmission electron microscopy (TEM). **(B)** Stopped-flow light scattering curves of pRPH- and pSPH-liposomes (LCR: 100) and DOPC liposome at ambient temperature. **(C)** The net water permeability of the liposomes. The inset presents an illustration of the fast water transport through a pRPH-liposome in stopped-flow experiments. **(D)** The activation energy (E_a) that is obtained from the linear regression of the best-fit lines in the Arrhenius plots. The draw solution in the stopped-flow tests is 600 mM sucrose.

energies (E_a) acquired from the Arrhenius plots (Fig. 2D) showed that the incorporation of the pRPH channels into the liposomes halved the activation energy from 10.9 kcal/mol (control liposome) to 5.4 kcal/-mol. In essence, the stopped-flow data and activation energy measurements provided solid evidence of water conveyance across the pRPH channel.

3.2. Characteristics of the control and biomimetic membranes

3.2.1. Physical characteristics

Fig. 3 presents the polyamide selective layer properties of the TFC control membrane and biomimetic membranes made with pRPH and pSPH channels at different loading concentrations. Close inspection of the surface morphologies and cross-sections in SEM revealed the typical ridge and valley structure that is reminiscence of the polyamide matrices synthesized using the MPD-TMC chemistry [5]. It is noticed that the polyamide features were larger and more noticeable for the biomimetic membranes. This was also corroborated by the much larger polyamide heights and surface roughness. For example, the polyamide heights of the NBM-pRPH-360 and NBM-pSPH-360 membranes were about ~23% larger than that of the TFC control membrane (175 nm), which is also manifested by the ~16% increase in surface roughness. Overall, we observed that polyamide matrices of NBM-pRPH-360 and NBM-pSPH-360 were fairly identical under a fixed channel concentration of 360 mg/L in MPD solution.

Upon further increase in the pRPH channel concentration in MPD solution (*i.e.,* NBM-pRPH-720), the polyamide protuberances were further enlarged, as per evidenced by the larger polyamide heights and roughness with respect to the NBM-pRPH-360 (Fig. 3D). Consequently, the much rougher polyamide surface of NBM-pRPH-720 led to an enhancement in the surface wettability (11% drop in contact angle). Overall, our results point to the fact the incorporation of pRPH led to larger protuberances and features that resulted in polyamides with larger heights and roughness. Here, we surmise that the pRPH channels do not function solely as a nanochannel in the IP process, but rather its presence could have affected the IP kinetics and polyamide formation. Also, the aggregation of pRPH channels under high concentrations (*e.g.* 720 mg/L) could have led to the formation of lumps of nanomaterials which resulted in a rougher and spatially thicker polyamide layer that has greater heights. In the current literature, many studies have also reported a similar trend whereby the addition of nanochannels or filler materials (such as I-quartets, metal-organic frameworks, or organic nanofillers) led to the evolution of polyamide layers with greater protuberances (that is manifested by greater heights and roughness) [32–35]. It is also worthy to note that the nanochannels were not directly observed in the SEM and TEM characterizations (refer to Figs. 2A and 3), presumably due to its small size (estimated to be <5 nm in length and ~0.5 nm in diameter) [19,20]. Therefore, it is not possible to obtain more information of the spatial orientation of the nanochannels in the polyamide layer. At the current stage, we postulate that the nanochannels were randomly positioned in the polyamide layer (analogous to the thin-film nanocomposite membranes incorporating carbon nanotubes) [36,37].

3.2.2. Chemical characteristics

Next, we attempted to study the changes in the polyamide chemistry of the SWRO membranes by examining their cross-linking degrees in the form of the O/N ratio obtained from XPS characterization experiments (here, the O/N ratio of 1 and 2 corresponds to a fully cross-linked and fully linear polyamide structure, respectively) [38]. First, Fig. 4A

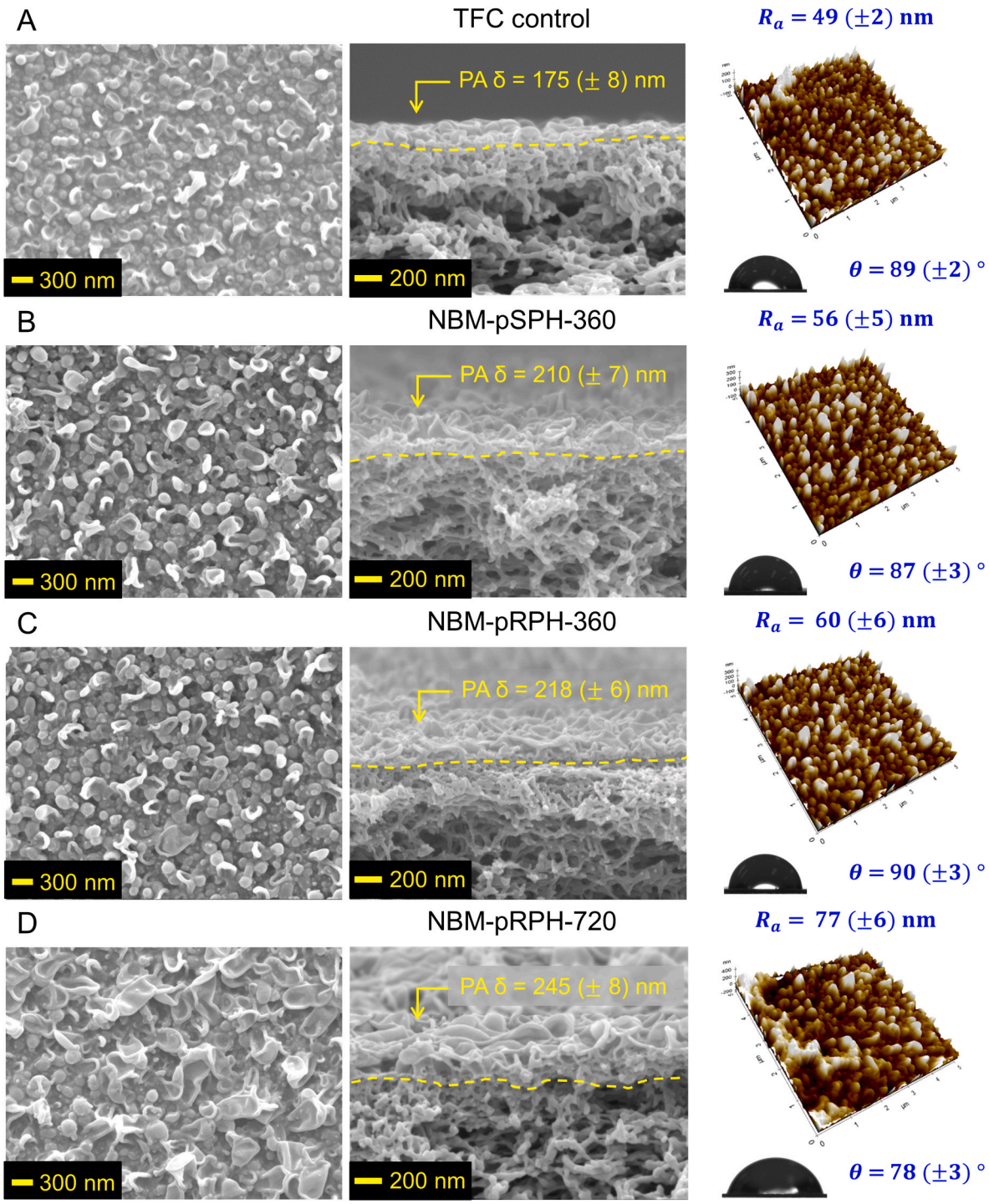

Fig. 3. The polyamide layer properties of the TFC control and biomimetic membranes incorporated different concentrations of nanochannels in MPD solution. **Leftmost panels:** SEM images displaying the surface morphologies. **Middle panels:** Cross-sectional SEM images with the selective layer height (δ). The yellow dashed line represents the boundary between the selective and support layers. **Rightmost panels:** 3D images from AFM with the roughness average (R_a) and equilibrium contact angle (θ) images obtained from the goniometer. (For interpretation of the references to color in this figure legend, the reader is referred to the Web version of this article.)

revealed that the cross-linking degree of the TFC control, NBM-pRPH-360 and NBM-pSPH-360 were fairly similar as per evidenced by their indistinguishable O/N ratios in XPS. This trend falls in line with the fairly similar intensity of the peak at 955 cm^{-1} in FTIR measurements (Fig. 4B), which reflects the amount of non-reacted acyl chlorides present in the polyamide matrices [27,39]. However, upon further increase in the pRPH channel loading rate, the intensity of the FTIR peak and O/N ratio of NBM-pRPH-720 showed discernible increases, which is reminiscence of a looser polyamide layer. Based on the characterization results, we surmised that the nanochannels did not alter the cross-ling degrees of the polyamide matrices to a large extent under a low nanochannel load (≤360 mg/L). However, at a high nanochannel loading rate of 720 mg/L, the pRPH channels could have agglomerated or influenced the IP formation mechanism by forming more voids in the polyamide matrices which consequently led to the formation of a looser polyamide matrix. This trend falls in line with the

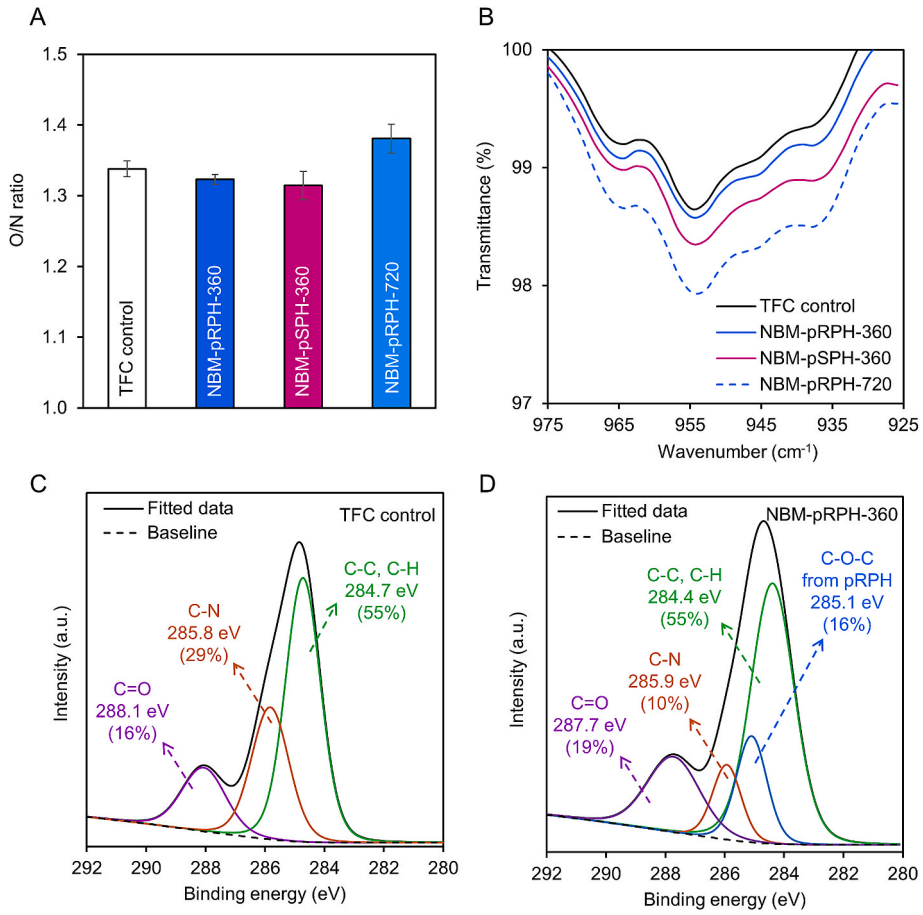

Fig. 4. (A) The O/N ratio obtained from XPS analyses. **(B)** The ATR-FTIR spectra outlining the intensity of the peak at 955 cm^{-1} for the control and biomimetic membranes. The FTIR spectra were obtained right after the curing stage in the membrane fabrication process. **(C and D)** The deconvoluted peaks of C1s in XPS for the TFC control and NBM-pRPH-360 membranes.

literature whereby the incorporation of nanomaterials (such as metal-organic frameworks (MOFs) or carbon materials) into polyamide matrices under high loading rates often resulted in a looser selective layer (*i.e.,* a reduced cross-linking degree) [35,40].

Besides deducing the changes in the cross-linking degrees of the polyamide layer, we also attempted to study the changes in chemical properties of the selective layers by quantifying the chemical bonds in the deconvoluted C1s narrow peak in XPS. According to the data presented in Fig. 4C, it is observed that the TFC control membrane consists of three peaks in the C1s narrow spectrum. According to previous reports, the leftmost peak at 288.1 eV is reminiscence of the strong electron-withdrawing groups in the polyamide layer (*e.g.,* O═C–O bonds in pendant carboxylic acid groups and O═C–N bonds in amides) [41]. Next, the intermediary peak at 285.8 eV is related to the weak electron withdrawing functional groups in the polyamide layer (*e.g.,* carbon atoms in C–N bond), whereas the rightmost peak at 284.7 eV is a manifestation of the pervasive C–H and C–C bonds in the polyamide matrices formed using the MPD-TMC chemistry [42]. Contrastingly, for the NBM-pRPH-360 membrane (Fig. 4D), besides the existence of these three peaks, it displayed one more distinctive peak at 285.1 eV as compared to the TFC membrane. According to the literature, this peak is affiliated with the presence of the C–O–C bonds (ether functional groups). Because the ether functional groups are only present in the pRPH compound (and not in polyamides), the unique peak at 285.1 eV is a proof of the successful incorporation of pRPH channels into the polyamide matrix [20]. Also, since XPS characterization analyzes the elemental compositions at the top surface of the polyamide layer (~5–10 nm) [27], the ether functional groups identified in Fig. 4D suggests the presence of the pRPH channels in the polyamide leaves. According to the literature, this observation is plausible, in which the nanomaterials are typically distributed in the topmost polyamide leaves and the core basal polyamide layer [43].

3.3. Desalination performances of the SWRO membranes

3.3.1. Closed-loop experiments and unraveling the water channel effect contributed by the pRPH channels

The desalination performance of the SWRO membranes is presented in Fig. 5A. It is noticed that all membranes were able to maintain decent NaCl rejections (>99.0%) in all experimental runs, suggesting their feasibility for SWRO desalination given that the membrane requirements for SWRO membranes are the more stringent than that of brackish water RO (BWRO) membranes. Moreover, the >99.0% NaCl rejection indicates that the incorporation of nanochannels did not compromise the polyamide integrity (*i.e.,* minimal defects were introduced), which is plausible given the small sizes of the nanochannels (<5 nm in length and ~0.5 nm in diameter) [20]. Hence, it is postulated that the nanochannels were fully integrated into the polyamide selective layer without any protrusions.

To unravel the water channel effect contributed by the pRPH channels, we attempted to scrutinize the membrane performances (Fig. 5A) in greater detail. Firstly, as compared to the TFC control membrane, we noticed that the membrane permeability gradually increased with pRPH loading in the MPD solution (from 0 to 360 mg/L). The NBM-pRPH-360 exhibited the best performance of 2.52 L m^{-2} h^{-1} bar^{-1}, which represents a 62% increment from the TFC control under a similar NaCl rejection of

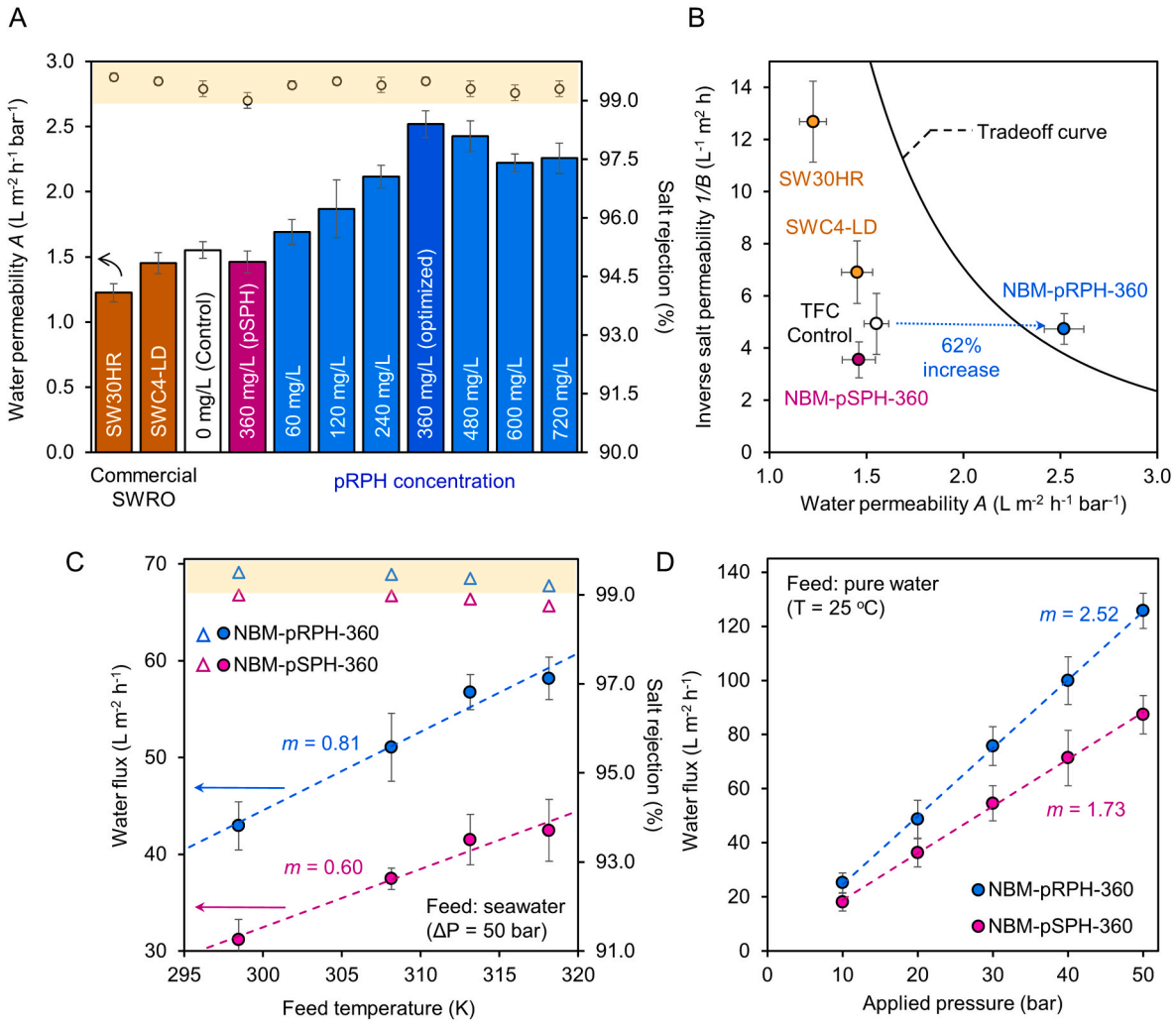

Fig. 5. (A) Experimental water permeability and salt rejection of NBM-pRPH membranes prepared from different pRPH concentrations in MPD solution (colored in blue). The performances of the two control membranes (TFC control and NBM-pSPH-360) and commercial SWRO membranes are presented for comparison purposes. The testing conditions were: 50 bar applied pressure, 32,000 mg/L NaCl as feed solution and 0% recovery (closed loop). **(B)** The plot of inverse salt permeability against water permeability for the tested membranes. The black solid curve represents the tradeoff relationship proposed in a recent work [5]. The effect of increasing temperatures **(C)** and pressures **(D)** on the performances of the NBM-pRPH-360 and NBM-pSPH-360 membranes. Both experiments were conducted in closed loop mode (0% recovery). For (C) ad (D), linear regression was performed to obtain the gradient of the line of best fit (*m*). (For interpretation of the references to color in this figure legend, the reader is referred to the Web version of this article.)

99.5%. Here, it is postulated that the enhanced permeability of the NBM-pRPH membranes arises from a polyamide that is rougher and with more voids (refer to Section 3.2.1) as well as the possible water transport pathways provided by the pRPH channels. In layman terms, we surmised that water transport in the biomimetic membrane can occur through two pathways: i) the pores of the pRPH channels and ii) the voids and free volume elements in the dense polyamide layer [44,45].

To narrow down on the permeability enhancement effect contributed

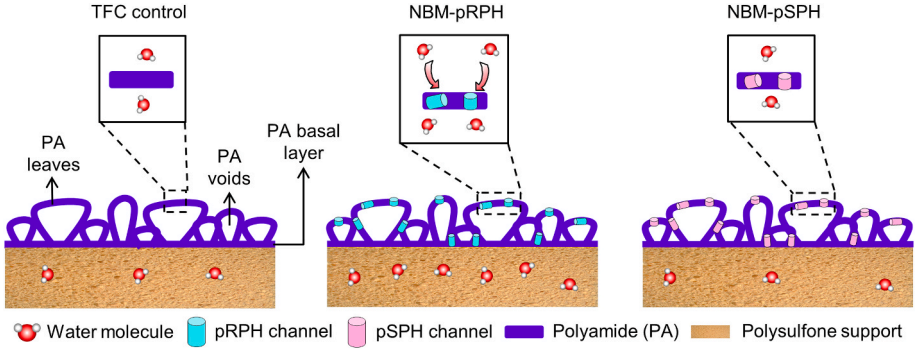

Fig. 6. Schematic illustrations of the supplementary water transport pathways provided by the pRPH channels in NBM-pRPH with respect to the TFC control and NBM-pSPH. It is surmised that the channels are randomly oriented in the polyamide layer.

by the pRPH channels, the performance of the NBM-pRPH-360 was directly compared with its mutant counterpart (*i.e.,* NBM-pSPH-360). Given that the physical and chemical characteristics of polyamide matrices are indistinguishable for NBM-pRPH-360 and NBM-pSPH-360 (refer to Section 3.2), we attribute the 70% enhanced permeability of NBM-pRPH-360 with respect to NBM-pSPH-360 to the favored water passage through the nanopore of the pRPH channels (as per confirmed in stopped-flow tests, refer to Section 3.1). In essence, the pRPH channels provide water molecules with a supplementary transport pathway with a reduced hydrodynamic resistance (Fig. 6). Coupled with its intrinsic ability to exclude monovalent ions (refer to Section 3.1), the presence of pRPH could enhance the SWRO membrane water permeability while maintaining its selectivity (99.5% NaCl rejection).

Secondly, we attempted to provide a stronger evidence of water transport across the pRPH channels by conducting RO tests under increasing feed temperatures and pressures. From the lines of best-fit presented in Fig. 5C, it is evident that the NBM-pRPH-360 showed a greater rate of flux rise with feed temperature as compared to its mutant counterpart, NBM-pSPH-360. Here, we surmised that the collision recurrence between the diffusing water molecules and pRPH's smooth interior cavity is decreased at higher temperatures thereby increasing the water transport rate. Together with the drop in water viscosity at elevated temperatures, the higher rate of flux rise for the NBM-pRPH-360 (with respect to NBM-pSPH-360) reveals potential water conveyance through the pRPH channels [20,46]. This trend was also observed in increasing pressure tests (Fig. 5D). The steeper best-fit line of NBM-pRPH-360 suggests expedited water transport because increasing ΔP supplies a greater driving force to overcome the entry barrier posed by the pRPH channels. In layman terms, this means that the extra kinetic energy supplied from the applied pressure allowed water molecules to overcome the entry resistance [20,46]. Consequently, water molecules transfused through the pRPH channels (as compared to pSPH), which is

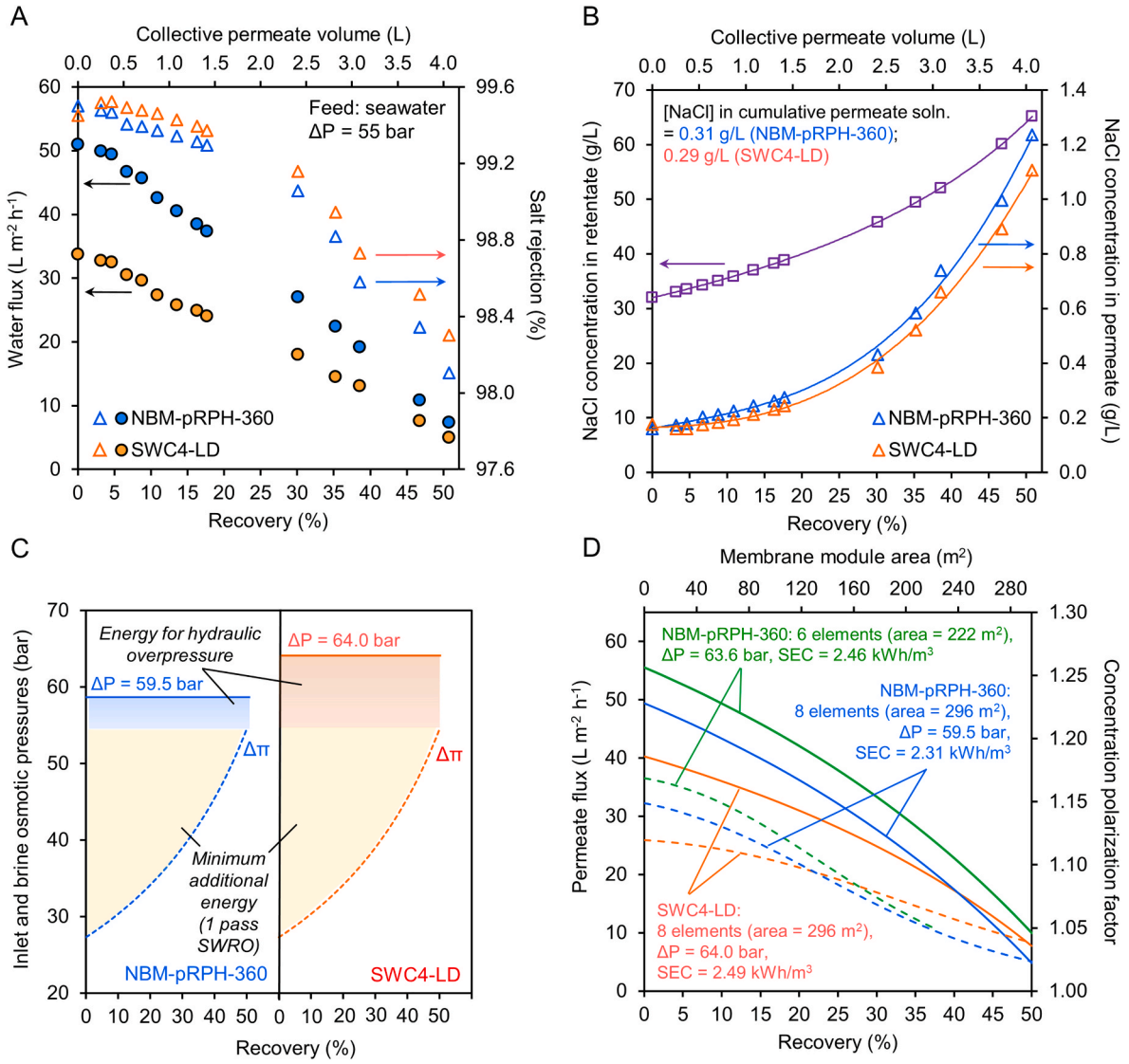

Fig. 7. (A and B) The plot of water flux, salt rejection and concentrations of the feed and permeate streams as a function of recovery (or collective permeate volume). The experiment was conducted in open-loop mode (target recovery of 50%) and the testing conditions were: constant applied pressure of 55 bar and 32,000 mg/L NaCl as feed solution. **(C)** The plot of brine osmotic pressure and applied pressure as a function of recovery. The minimum additional energy represents the irreversible losses in a one-pass SWRO (yellow area) whereas the hydraulic overpressure is needed to achieve the pre-determined recovery. **(D)** The profile of permeate flux within an SWRO module (*i.e.,* a single train) as a function recovery (solid lines) and the concentration polarization factor as a function of cumulative membrane area (dashed lines). Note: For (C–D), the performances were obtained *via* module-scale modeling of an SWRO system consisting of spiral-wound membrane elements connected in series (refer to Section 2.7 for the simulation methodology). (For interpretation of the references to color in this figure legend, the reader is referred to the Web version of this article.)

a good indirect corroboration of water transport through the pRPH channels.

Thirdly, it can be observed that the water permeability of the NBM-pRPH membranes begin to drop when the concentration of pRPH is further increased beyond 360 mg/L (*e.g.,* NBM-pRPH-720 exhibited a 10% decrease in permeability when compared against NBM-pRPH-360). We postulated that the channels could have aggregated under higher concentrations to form agglomerated clusters [33,40,47]. This means that water transport does not occur through all nanochannels, thereby reducing the number of nanopore available for water transport through the polyamide layer. In light of this proposition, the water permeability of NBM-pRPH membranes did not increase linearly beyond the optimal loading of 360 mg/L in MPD solution.

3.3.2. Quantifying the energy and footprint savings achievable by NBM-pRPH-360

Among the various approaches to fabricate high-performance SWRO membranes, our method offers an opportunity in large-scale membrane fabrication due to its convenient adaption into the industrial IP process, in which pRPH channels are directly blended into the MPD solution prior to IP (*e.g.,* by retrofitting the existing fabrication lines) [48]. In this section, we first study the performance of the optimized NBM-pRPH-360 membrane in high recovery experiments, representative of conditions in actual desalination plants [49]. The state-of-the-art commercial SWC4-LD membrane was tested in parallel for benchmarking purposes. The experiment was conducted under 50% recovery using seawater as feed under an applied pressure of 55 bar. According to the trends presented in Fig. 7A, the NBM-pRPH-360 membrane showed 51% higher water flux than SWC4-LD at the initial stage with a similar salt rejection of 99.5%. However, the trends of the permeate flux and salt rejection for both membranes gradually decrease with recovery due to the reduction in driving force (*i.e.,* hydraulic overpressure) as the feed solution became more concentrated (Fig. 7B). Overall, the concentration of permeate collected using the NBM-pRPH-360 membrane (0.31 g/L) was fairly like that of SWC4-LD (0.29 g/L). These values fulfill the criteria for set forth by the World Health Organization for drinking water quality [50], thereby affirming the promising performances of the NBM-pRPH-360 membrane in actual desalination.

In summary, the NBM-pRPH-360 membrane could produce more water than the SWC4-LD membrane under a similar permeate quality when tested under identical conditions. Coupled with the large scale-up potential of our biomimetic membrane, we attempted to estimate the benefits which NBM-pRPH-360 could bring about at the system-level. Herein, we quantify the energy and footprint savings attainable by the optimized NBM-pRPH-360 membrane in an actual desalination process by extending a recent modelling work by our research group (readers are referred to Ref. [31] for detailed information as well as model validation). By modeling the fluid dynamics and mass transport in an SWRO train (consisting of several spiral-wound elements connected in series), we calculated the SEC and footprint of the membrane unit stage in SWRO. Based on the results presented in Fig. 7C, it is evident that a desalination process adopting both membranes would require more energy than would be required by thermodynamics (applied pressure is 9% and 17% above the brine osmotic pressure for NBM-pRPH-360 and SWC4-LD, respectively). This is plausible given that the performance standards of both membranes is below the thermodynamic limit for spiral-wound SWRO membranes (3 L m^{-2} h^{-1} bar^{-1}) [31].

In terms of footprint savings, our modelling results suggest that under the similar applied pressure of ~64 bar, the NBM-pRPH-360 could achieve 50% recovery of permeate water with six elements instead of eight elements that is needed by the commercial SWC4-LD membrane (Fig. 7D). In layman terms, the larger water permeability of the NBM-pRPH-360 membrane would reduce the required membrane area by 25% (from 296 m^2 to 222 m^2), translating to proportional savings in terms of footprint (which includes capital and membrane replacement costs). On the other hand, an alternative configuration can involve the same membrane area (that is, the same number of elements with respect to SWC4-LD), and the NBM-pRPH-360 membrane would reduce the applied pressure required from 64.0 bar to 59.5 bar. This would translate to a noteworthy 7.2% reduction in SEC with respect to SWC4-LD while producing the same amount of freshwater. Finally, it is also noticed that the concentration polarization factor of the SWRO membranes were lower than 1.20, which shows that concentration polarization is still well controlled within the current flux range [51]. Overall, our results suggest that concentration polarization does not seem to nullify the benefits which the NBM-pRPH-360 can bring about due to its greater productivity, as per evidenced by the significant energy and membrane area savings which it could achieve with respect to the commercial SWC4-LD membrane. Future works could also use molecular dynamics simulations to predict the fouling potential of our membranes to include the impact of progressive membrane fouling in the system-level modelling [31,52].

3.3.3. Chemical stability and mechanical durability of NBM-pRPH-360

In this section, we attempted to elucidate the resilience of the optimized NBM-pRPH-360 membrane when subjected to chemical and mechanical stress (Fig. 8A and B). Firstly, it is noticed that our SWRO membranes exhibited a plastic behavior (that is, the irreversible and permanent reduction of free volumes in the polyamide) after compaction whereby they could not recover their original permeability values at low pressures. We conjectured that the incorporation of nanochannels into the selective layer did not compromise the polyamide integrity, since the extent of permeability reduction after compaction is fairly similar to that of the control membrane (refer to Fig. 8B). Here, it is noticed that the membranes retained their permeability values after compaction that is manifested by the similar performances after the applied pressure was gradually decreased. The desalination performances of the NBM-pRPH-360 membrane also remained relatively stable after stability and durability tests under SWRO conditions. As shown in Fig. 8A, the water flux of the NBM-pRPH-360 membrane retained ~90% of its original value (43 L m^{-2} h^{-1}) after two days of SWRO compaction as well as individually being subjected to various cleaning agents containing acids, bases, and amphiphilic compounds (*e.g.,* SDS surfactant) [29,30]. More importantly, besides the ability to maintain the water flux, the selectivity of the NBM-pRPH-360 was not compromised, as per evidenced by the salt rejections of ~99.0–99.5%. This confirms the robustness of our NBM-pRPH-360 membrane for practical desalination operations (*e.g.,* when subjected to chemical cleaning or in the handling of feed water with high temperatures).

Lastly, we also conducted a seven-day test using real seawater feed to examine the feasibility of the NBM-pRPH-360 membrane in desalinating real seawater (Fig. 8C). For comparison purposes, the commercial SWC4-LD membrane was tested in parallel under identical conditions. Throughout the seven-day test, it is noticed that the water flux of the NBM-pRPH-360 membrane showed a 10% drop from its initial value after two days of operation. Thereafter, the water flux stabilized and remained fairly consistent at 41.5 L m^{-2} h^{-1}, which was 28% higher than that of SWC4-LD (32.5 L m^{-2} h^{-1}) under fairly similar rejection of ~99.3% (refer to Fig. 8C and Table 1). Lastly, we also examined the ionic concentrations of the permeate water that were obtained from the NBM-pRPH-360 membrane. It is observed that our membrane showed fairly similar rejection of monovalent and divalent ions to that of SWC4-LD (Table 1), indicating the feasibility of our membrane for practical desalination application. However, we also note that the boron rejection of the NBM-pRPH-360 falls short of that achievable by SWC4-LD by about 7%. Thus, future works could involve the use of surface coating or modification of the polyamide chemistry to further improve the boron rejection of NBM-pRPH-360 [60,61].

Overall, our biomimetic membranes incorporating pRPH channels presents a feasible alternative in the fabrication of high-performance SWRO membranes with performance standards matching those of other thin-film nanocomposite (TFN) SWRO membranes incorporated

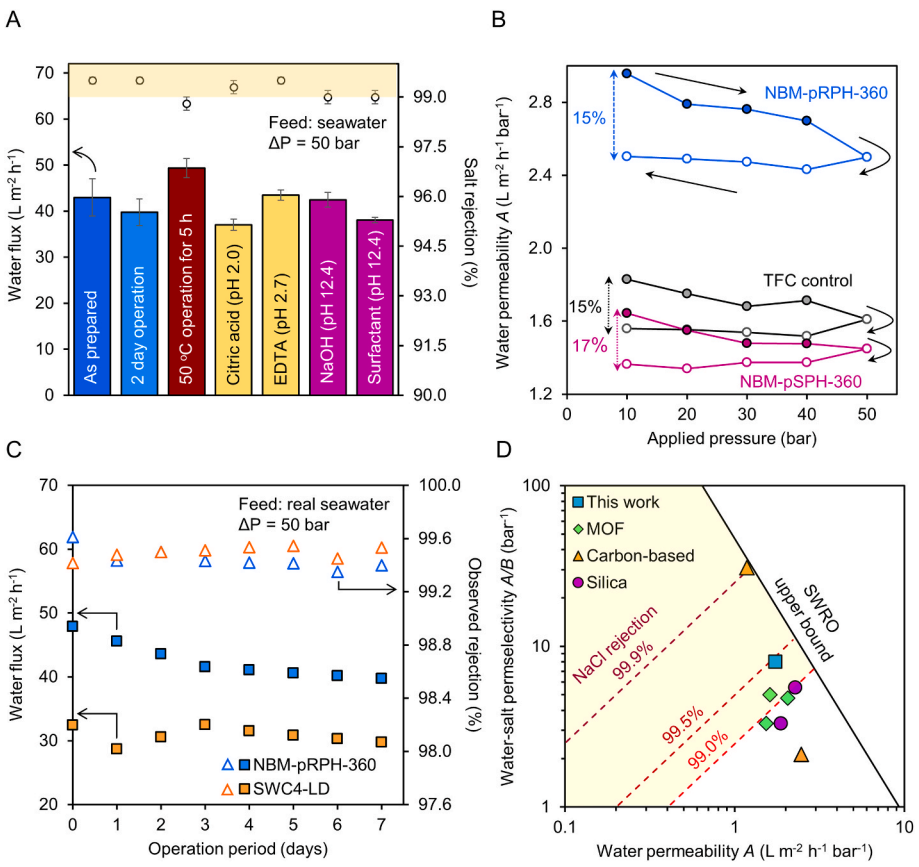

Fig. 8. (A) The desalination performances of the NBM-pRPH-360 membrane after being subjected to chemical stresses and compaction. The testing conditions were: 50 bar applied pressure, 32,000 mg/L NaCl as feed solution and 0% recovery (closed loop). **(B)** The plot of permeability against applied pressure of the SWRO membranes. The pressure was gradually stepped-up till 50 bar (marked by solid points) and then gradually stepped down to 10 bar (marked by dotted points). **(C)** The desalination performance of the NBM-pRPH-360 and commercial SWC4-LD membranes in a seven-day test. The testing conditions were: 50 bar applied pressure and 0% recovery (closed loop) using real seawater feed. **(D)** The plot of water-salt permselectivity against salt water permeability for different types of nanomaterial-embedded SWRO membranes. The SWRO upper-bound line was adapted from Ref. [5], with the area underneath divided into three regions corresponding to different NaCl rejections, at an SWRO water flux of 40 L m^{-2} h^{-1}. The data points in the graph include recent works of SWRO membranes incorporated with carbon nanomaterials [53,54], metal-organic frameworks (MOFs) [55–57] and silica nanoparticles [58,59].

Table 1
The measured ionic composition of the real seawater feed and permeate water of NBM-pRPH-360 and commercial SWC4-LD membranes. The observed rejections of the individual ions and total dissolved solids (TDS) are tabulated.

		NBM-pRPH-360		Commercial SWC4-LD	
Ions or parameter	Feed concentration (mg/L)	Permeate concentration (mg/L)	Solute rejection (%)	Permeate concentration (mg/L)	Solute rejection (%)
Na^+	8509	59.3	99.3	51.5	99.4
Mg^{2+}	1043	1.16	99.9	1.86	99.8
K^+	260	1.52	99.4	1.70	99.3
Ca^{2+}	325	0.66	99.8	0.44	99.9
B	4.6	0.86	81.3	0.51	88.9
Cl^-	17262	94.3	99.5	86.2	99.5
Br^-	34.3	0.18	99.5	0.19	99.4
SO_4^{2-}	2056	1.05	99.9	3.32	99.8
TDS	29646	163	99.5	132	99.6
Conductivity (μs/cm)	44850	330.1	99.3	267.2	99.4
pH	8.16	7.45	–	7.53	–

with filler nanomaterials (Fig. 8D). The principal similarity between our work and the literature is that the nanomaterials are dispersed in the polyamide selective layer, and it is hypothesized that the intrinsic cavity of the nanochannels provides supplementary transport pathways that enable the selective transport of water over solutes. However, the formation of defects is still a persistent issue, which necessitates the use of ultrasonication and material functionalization to enable the nanomaterials to be well dispersed in the monomeric solutions in IP. One crucial advantage of pillar[5]arene channels is that its appending groups could be functionalized to enable it to be water-soluble [62], which will consequently ensure its excellent dispersibility in the MPD solution. We surmise that this trait is crucial for that a homogeneous dispersion of nanochannels in IP monomeric solutions is a pre-requisite to fabricate defect-free selective layers that will enable the SWRO membrane to achieve high salt rejections ≥99.5% [5,63].

4. Conclusions

This work demonstrates the possibility to directly incorporate and disperse pRPH water channels into the polyamide selective layer of SWRO membranes. The optimized membrane, NBM-pRPH-360 showed a 62% permeability improvement with reference to the pristine control under SWRO testing conditions of 50 bar applied pressure and feed salinity of 32,000 ppm NaCl. This work illustrates a straightforward method for fabricating SWRO NBMs and has huge potential for scale-up production by retrofitting existing IP fabrication lines. The key highlights of this paper are presented as follows:

(1) The biomimetic SWRO membrane prepared with a pRPH concentration of 360 mg/L in MPD solution exhibited the optimized performance of 2.52 L m^{-2} h^{-1} bar^{-1} with 99.5% NaCl rejection in SWRO conditions.

(2) The direct comparison with the mutant version (NBM-pSPH-360) with fairly similar polyamide matrices suggested the possible water conveyance through the pRPH channels.
(3) The module-scale modelling results suggest that the NBM-pRPH-360 membrane can reduce the SEC of the SWRO membrane unit stage by 7.2% (or reduce the required membrane area by 25%) with respect to SWC4-LD under a similar water production rate.
(4) In a one-week test conducted using actual seawater feed, our NBM-pRPH-360 membrane exhibited a stable flux of 42 L m^{-2} h^{-1}, which was 28% higher than that of the commercial SWC4-LD membrane with comparable solute rejection of 99.3%.

Authors statement

Yu Jie Lim: Conceptualization, Investigation, Data curation, Writing - Original Draft.
Gwo Sung Lai: Conceptualization, Methodology, Resources.
Yali Zhao: Conceptualization, Methodology, Resources.
Yunqiao Ma: Conceptualization, Methodology, Resources.
Jaume Torres: Supervision.
Rong Wang: Supervision, Writing - review & editing, Project administration, Funding acquisition.

Declaration of competing interest

The authors declare that they have no known competing financial interests or personal relationships that could have appeared to influence the work reported in this paper.

Data availability

Data will be made available on request.

Acknowledgements

Firstly, we would like to thank Mr. Song Zhijian and Mr. Keng Wai Ren from the Singapore Membrane Technology Centre, Nanyang Technological University, Singapore, for helping with channel synthesis and ICP experiments, respectively. Secondly, we would like to acknowledge Ms. Lam Mei Shan from NEWRI Analytics Cluster, Nanyang Technological University, Singapore, for helping with TEM characterization experiments. This research grant is administered by PUB, Singapore's National Water Agency (grant number: PUB-1800-0010) and supported by the Singapore National Research Foundation under its Environment and Water Research Program.

References

[1] Y.J. Lim, K. Goh, R. Wang, The coming of age of water channels for separation membranes: from biological to biomimetic to synthetic, Chem. Soc. Rev. 51 (2022) 4537–4582.
[2] X. Han, Y. Wang, Z. Wang, X. Li, Y. Liu, C. Wang, F. Yan, J. Wang, Interfacial polymerization plus: a new strategy for membrane selective layer construction, J. Membr. Sci. 642 (2022), 119973.
[3] X. Li, Z. Wang, X. Han, Y. Liu, C. Wang, F. Yan, J. Wang, Regulating the interfacial polymerization process toward high-performance polyamide thin-film composite reverse osmosis and nanofiltration membranes: a review, J. Membr. Sci. 640 (2021), 119765.
[4] Y. Li, T.-H. Chen, C.-Y. Yu, T. Wu, X.-T. Zhao, J.-F. Pan, L.-F. Liu, Facile polyamide microstructure adjustment of the composite reverse osmosis membrane assisted by PF127/SDS mixed micelles for improving seawater desalination performance, Desalination 521 (2022), 115395.
[5] Y.J. Lim, K. Goh, M. Kurihara, R. Wang, Seawater desalination by reverse osmosis: current development and future challenges in membrane fabrication–A review, J. Membr. Sci. 629 (2021), 119292.
[6] R.S. Kingsbury, J. Wang, O. Coronell, Comparison of water and salt transport properties of ion exchange, reverse osmosis, and nanofiltration membranes for desalination and energy applications, J. Membr. Sci. 604 (2020), 117998.
[7] L. Xu, B. Shan, C. Gao, J. Xu, Multifunctional thin-film nanocomposite membranes comprising covalent organic nanosheets with high crystallinity for efficient reverse osmosis desalination, J. Membr. Sci. 593 (2020), 117398.
[8] A. Raza, J.Z. Hassan, A. Mahmood, W. Nabgan, M. Ikram, Recent advances in membrane-enabled water desalination by 2D frameworks: graphene and beyond, Desalination 531 (2022), 115684.
[9] Y. Liu, M.-O. Coppens, Z. Jiang, Mixed-dimensional membranes: chemistry and structure–property relationships, Chem. Soc. Rev. 50 (2021) 11747–11765.
[10] X.-L. Cao, J.-L. Guo, J. Cai, M.-L. Liu, S. Japip, W. Xing, S.-P. Sun, The encouraging improvement of polyamide nanofiltration membrane by cucurbituril-based host–guest chemistry, AlChE J 66 (2020), e16879.
[11] L. Cheng, G. Liu, J. Zhao, W. Jin, Two-Dimensional-material membranes: manipulating the transport pathway for molecular separation, Acc. Mater. Res. 2 (2021) 114–128.
[12] Y.-M. Tu, L. Samineni, T. Ren, A.B. Schantz, W. Song, S. Sharma, M. Kumar, Prospective applications of nanometer-scale pore size biomimetic and bioinspired membranes, J. Membr. Sci. 620 (2020), 118968.
[13] J. Shen, G. Liu, Y. Han, W. Jin, Artificial channels for confined mass transport at the sub-nanometre scale, Nat. Rev. Mater. 6 (2021) 294–312.
[14] M. Zhang, P. Zhao, P. Li, Y. Ji, G. Liu, W. Jin, Designing biomimic two-dimensional ionic transport channels for efficient ion sieving, ACS Nano 15 (2021) 5209–5220.
[15] W. Chen, P. Chen, G. Zhang, G. Xing, Y. Feng, Y.-W. Yang, L. Chen, Macrocycle-derived hierarchical porous organic polymers: synthesis and applications, Chem. Soc. Rev. 50 (2021) 11684–11714.
[16] Y.-x. Shen, W. Song, D.R. Barden, T. Ren, C. Lang, H. Feroz, C.B. Henderson, P. O. Saboe, D. Tsai, H. Yan, P.J. Butler, G.C. Bazan, W.A. Phillip, R.J. Hickey, P. S. Cremer, H. Vashisth, M. Kumar, Achieving high permeability and enhanced selectivity for Angstrom-scale separations using artificial water channel membranes, Nat. Commun. 9 (2018) 1–11.
[17] H. Zhang, X. Li, J. Hou, L. Jiang, H. Wang, Angstrom-scale ion channels towards single-ion selectivity, Chem. Soc. Rev. 51 (2022) 2224–2254.
[18] Z.-J. Yan, D. Wang, Z. Ye, T. Fan, G. Wu, L. Deng, L. Yang, B. Li, J. Liu, T. Ma, C. Dong, Z.-T. Li, L. Xiao, Y. Wang, W. Wang, J.-L. Hou, Artificial aquaporin that restores wound healing of impaired cells, J. Am. Chem. Soc. 142 (2020) 15638–15643.
[19] Q. Li, X. Li, L. Ning, C.H. Tan, Y. Mu, R. Wang, Hyperfast water transport through biomimetic nanochannels from peptide-attached (pR)-pillar[5]arene, Small 15 (2019), 1804678.
[20] Y.J. Lim, K. Goh, G.S. Lai, C.Y. Ng, J. Torres, R. Wang, Fast water transport through biomimetic reverse osmosis membranes embedded with peptide-attached (pR)-pillar[5]arenes water channels, J. Membr. Sci. 628 (2021), 119276.
[21] K. Kato, S. Fa, S. Ohtani, T.-h. Shi, A.M. Brouwer, T. Ogoshi, Noncovalently bound and mechanically interlocked systems using pillar[n]arenes, Chem. Soc. Rev. 51 (2022) 3648–3687.
[22] G.T. Williams, C.J.E. Haynes, M. Fares, C. Caltagirone, J.R. Hiscock, P.A. Gale, Advances in applied supramolecular technologies, Chem. Soc. Rev. 50 (2021) 2737–2763.
[23] Y.J. Lim, S.M. Lee, R. Wang, J. Lee, Emerging materials to prepare mixed matrix membranes for pollutant removal in water, Membranes 11 (2021) 508.
[24] Y. Zhao, G.S. Lai, Y. Wang, C. Li, R. Wang, Impact of pilot-scale PSF substrate surface and pore structural properties on tailoring seawater reverse osmosis membrane performance, J. Membr. Sci. 633 (2021), 119395.
[25] S. Habib, S.T. Weinman, A review on the synthesis of fully aromatic polyamide reverse osmosis membranes, Desalination 502 (2021), 114939.
[26] Z. Wang, S. Liang, Y. Kang, W. Zhao, Y. Xia, J. Yang, H. Wang, X. Zhang, Manipulating interfacial polymerization for polymeric nanofilms of composite separation membranes, Prog. Polym. Sci. 122 (2021), 101450.
[27] Y.J. Lim, K. Goh, G.S. Lai, Y. Zhao, J. Torres, R. Wang, Unraveling the role of support membrane chemistry and pore properties on the formation of thin-film composite polyamide membranes, J. Membr. Sci. 640 (2021), 119805.
[28] N.A. Pham, D.Y.F. Ng, K. Goh, Z. Dong, R. Wang, Assessing the potential of integrally skinned asymmetric hollow fiber membranes for addressing membrane fouling in pressure retarded osmosis process, Desalination 520 (2021), 115347.
[29] H. Chu, J. Ma, X. Liu, F. Wang, X. Zhou, Y. Zhang, E. Li, X. Zhang, Spatial evolution of membrane fouling along a multi-stage integrated membrane system: a pilot study for steel industry brine recycling, Desalination 527 (2022), 115566.
[30] Y.-G. Lee, S. Kim, J. Shin, H. Rho, Y.M. Kim, K.H. Cho, H. Eom, S.-E. Oh, J. Cho, K. Chon, Sequential effects of cleaning protocols on desorption of reverse osmosis membrane foulants: autopsy results from a full-scale desalination plant, Desalination 500 (2021), 114830.
[31] Y.J. Lim, Y. Ma, J.W. Chew, R. Wang, Assessing the potential of highly permeable reverse osmosis membranes for desalination: specific energy and footprint analysis, Desalination 533 (2022), 115771.
[32] M. Di Vincenzo, A. Tiraferri, V.-E. Musteata, S. Chisca, R. Sougrat, L.-B. Huang, S. P. Nunes, M. Barboiu, Biomimetic artificial water channel membranes for enhanced desalination, Nat. Nanotechnol. 16 (2020) 190–196.
[33] Y. Liu, X.-p. Wang, Z.-a. Zong, R. Lin, X.-y. Zhang, F.-s. Chen, W.-d. Ding, L.-l. Zhang, X.-m. Meng, J. Hou, Thin film nanocomposite membrane incorporated with 2D-MOF nanosheets for highly efficient reverse osmosis desalination, J. Membr. Sci. 653 (2022), 120520.
[34] G.S. Lai, Y. Zhao, R. Wang, Liposome-integrated seawater reverse osmosis membrane prepared via facile spray-assisted interfacial polymerization, J. Membr. Sci. 650 (2022), 120405.
[35] Y. Wang, H. Zhang, C. Song, C. Gao, G. Zhu, Effect of aminophend/formaldehyde resin polymeric nanospheres as nanofiller on polyamide thin film nanocomposite membranes for reverse osmosis application, J. Membr. Sci. 614 (2020), 118496.
[36] A. Güvensoy-Morkoyun, S. Kürklü-Kocaoğlu, C. Yıldırım, S. Velioğlu, H. E. Karahan, T.-H. Bae, Ş.B. Tantekin-Ersolmaz, Carbon nanotubes integrated into

polyamide membranes by support pre-infiltration improve the desalination performance, Carbon 185 (2021) 546–557.
[37] A. Zhao, N. Zhang, Q. Li, L. Zhou, H. Deng, Z. Li, Y. Wang, E. Lv, Z. Li, M. Qiao, J. Wang, Incorporation of silver-embedded carbon nanotubes coated with tannic acid into polyamide reverse osmosis membranes toward high permeability, antifouling, and antibacterial properties, ACS Sustainable Chem. Eng. 9 (2021) 11388–11402.
[38] Y.J. Lim, J. Lee, T.-H. Bae, J. Torres, R. Wang, Feasibility and performance of a thin-film composite seawater reverse osmosis membrane fabricated on a highly porous microstructured support, J. Membr. Sci. 611 (2020), 118407.
[39] J. Lee, Y.J. Lim, J.H. Low, S.M. Lee, C.-H. Lee, R. Wang, T.-H. Bae, Synergistic effect of highly porous microstructured support and co-solvent assisted interfacial polymerization on the performance of thin-film composite FO membranes, Desalination 539 (2022), 115947.
[40] F. Asempour, S. Akbari, M.H. Kanani-Jazi, A. Atashgar, T. Matsuura, B. Kruczek, Chlorine-resistant TFN RO membranes containing modified poly(amidoamine) dendrimer-functionalized halloysite nanotubes, J. Membr. Sci. 623 (2021), 119039.
[41] X. Li, Z. Wang, X. Han, J. Wang, Facile fabrication of hydroxyl-rich polyamide TFC RO membranes for enhanced boron removal performance, Desalination 531 (2022), 115723.
[42] H. Zheng, Z. Mou, K. Zhou, Incorporation of core–shell-structured zwitterionic carbon dots in thin-film nanocomposite membranes for simultaneously improved perm-selectivity and antifouling properties, ACS Appl. Mater. Interfaces 12 (2020) 53215–53229.
[43] X. Qian, X. Wang, X. Gao, W. Cao, C. Gao, Effects of GO@CS core-shell nanomaterials loading positions on the properties of thin film nanocomposite membranes, J. Membr. Sci. 624 (2021), 119102.
[44] V. Freger, G.Z. Ramon, Polyamide desalination membranes: formation, structure, and properties, Prog. Polym. Sci. 122 (2021), 101451.
[45] H. Zheng, Z. Mou, Y.J. Lim, N. Srikanth, W. Zhang, S. Guo, R. Wang, K. Zhou, High-precision and high-flux separation by rationally designing the nanochannels and surface nanostructure of polyamide nanofiltration membranes, Small Science 2 (2022), 2200026.
[46] D. Chen, Q. Liang, F. Gao, T. Liu, Y. Wu, Z. Zheng, J. Kang, R. Xu, Y. Cao, M. Xiang, Design of high-performance biomimetic reverse osmosis membranes by introducing loose liposome as an artificial water channel, Chem. Eng. J. 431 (2022), 133878.
[47] S. Jeon, S.S. Shin, C.H. Park, J.-H. Lee, Star polymer-mediated in-situ synthesis of silver-incorporated reverse osmosis membranes with excellent and durable biofouling resistance, J. Membr. Sci. 639 (2021), 119778.
[48] Z. Kang, H. Guo, L. Fan, G. Yang, Y. Feng, D. Sun, S. Mintova, Scalable crystalline porous membranes: current state and perspectives, Chem. Soc. Rev. 50 (2021) 1913–1944.
[49] C. Skuse, A. Gallego-Schmid, A. Azapagic, P. Gorgojo, Can emerging membrane-based desalination technologies replace reverse osmosis? Desalination 500 (2021), 114844.
[50] J. Bundschuh, M. Kaczmarczyk, N. Ghaffour, B. Tomaszewska, State-of-the-art of renewable energy sources used in water desalination: present and future prospects, Desalination 508 (2021), 115035.
[51] Z. Zhou, B. Ling, I. Battiato, S.M. Husson, D.A. Ladner, Concentration polarization over reverse osmosis membranes with engineered surface features, J. Membr. Sci. 617 (2021), 118199.
[52] Y. Ma, J.W. Chew, Investigation of membrane fouling phenomenon using molecular dynamics simulations: a review, J. Membr. Sci. 661 (2022), 120874.
[53] H. Zhang, Y. Wang, Y. Wei, C. Gao, G. Zhu, Fabrication of polyamide thin film nanocomposite reverse osmosis membrane incorporated with a novel graphite-based carbon material for desalination, J. Appl. Polym. Sci. 137 (2020), 49030.
[54] J.L. Fajardo-Diaz, A. Morelos-Gomez, R. Cruz-Silva, A. Matsumoto, Y. Ueno, N. Takeuchi, K. Kitamura, H. Miyakawa, S. Tejima, K. Takeuchi, K. Tsuzuki, M. Endo, Antifouling performance of spiral wound type module made of carbon nanotubes/polyamide composite RO membrane for seawater desalination, Desalination 523 (2022), 115445.
[55] Q. Zhao, D.L. Zhao, T.-S. Chung, Thin-film nanocomposite membranes incorporated with defective ZIF-8 nanoparticles for brackish water and seawater desalination, J. Membr. Sci. 625 (2021), 119158.
[56] L. Liu, X. Xie, S. Qi, R. Li, X. Zhang, X. Song, C. Gao, Thin film nanocomposite reverse osmosis membrane incorporated with UiO-66 nanoparticles for enhanced boron removal, J. Membr. Sci. 580 (2019) 101–109.
[57] D.L. Zhao, W.S. Yeung, Q. Zhao, T.-S. Chung, Thin-film nanocomposite membranes incorporated with UiO-66-NH2 nanoparticles for brackish water and seawater desalination, J. Membr. Sci. 604 (2020), 118039.
[58] B. Wu, S. Wang, J. Wang, X. Song, Y. Zhou, C. Gao, Facile fabrication of high-performance thin film nanocomposite desalination membranes imbedded with alkyl group-capped silica nanoparticles, Polymers 12 (2020) 1415.
[59] J. Wang, Q. Wang, X. Gao, X. Tian, Y. Wei, Z. Cao, C. Guo, H. Zhang, Z. Ma, Y. Zhang, Surface modification of mesoporous silica nanoparticle with 4-triethoxysilylaniline to enhance seawater desalination properties of thin-film nanocomposite reverse osmosis membranes, Front. Environ. Sci. Eng. 14 (2020) 6.
[60] S. Wang, S. Bing, H. Zhang, Y. Zhou, L. Zhang, C. Gao, Surface engineering design of polyamide membranes for enhanced boron removal in seawater desalination, J. Membr. Sci. 651 (2022), 120425.
[61] Y. Li, S. Wang, X. Song, Y. Zhou, H. Shen, X. Cao, P. Zhang, C. Gao, High boron removal polyamide reverse osmosis membranes by swelling induced embedding of a sulfonyl molecular plug, J. Membr. Sci. 597 (2020), 117716.
[62] T. Wang, C. Ménard-Moyon, A. Bianco, Self-assembly of amphiphilic amino acid derivatives for biomedical applications, Chem. Soc. Rev. 51 (2022) 3535–3560.
[63] Y. Li, N. Li, Y. Xia, S. Yuan, X. Zhang, Tailoring the physicochemical and geometric properties of two-dimensional graphene membranes for aqueous separation, Desalination 530 (2022), 115621.